Role of gravity waves in the spatial and temporal variability of stratospheric temperature measured by COSMIC/FORMOSAT-3 and Rayleigh lidar observations

Adrian J. McDonald,[1] Bo Tan,[2,3] and Xinzhao Chu[2,3]

Received 3 December 2009; revised 14 April 2010; accepted 20 April 2010; published 15 October 2010.

[1] This study utilizes COSMIC satellite and lidar observations to examine the spatial and temporal variability of stratospheric temperature at a number of scales. The geographic variation of the RMS temperature difference between pairs of COSMIC profiles shows a strong correspondence to previous climatologies of gravity wave activity. In addition, the second-order structure functions we form can be directly related to the horizontal wave number power spectrum. These structure functions for different seasons and altitudes display a close correspondence to previous studies which examined the form of the horizontal wave number power spectra. Our analysis suggests that the wavefield may be particularly affected by changes in the zonal wind between 15 and 25 km and that the wind reversal between tropospheric westerlies and stratospheric easterlies in summer strongly contributes to critical-level filtering. Inspection also shows that longer horizontal wavelength waves are preferentially removed in this region. At low altitudes, the variability related to gravity waves shows a remarkably similar pattern as a function of horizontal separation in both hemispheres but is quite different at higher altitudes. Such contrast implies that seasonal variability at higher altitudes may be dominated by changes in propagation conditions in the lower stratosphere. Examination of temperature variability as a function of spatial and temporal separation indicates that gravity wave activity dominates stratospheric temperature variability, and this has impacts on validation study site selection. For example, validation exercises in the summer hemisphere stratosphere are likely to be less affected by geophysical variability than those in the winter hemisphere.

Citation: McDonald, A. J., B. Tan, and X. Chu (2010), Role of gravity waves in the spatial and temporal variability of stratospheric temperature measured by COSMIC/FORMOSAT-3 and Rayleigh lidar observations, *J. Geophys. Res.*, *115*, D19128, doi:10.1029/2009JD013658.

1. Introduction

[2] The aim of this study is to examine the variation of stratospheric temperature as a function of spatial and temporal separation. Characterization of these variations has two important uses; first, the small-scale variations examined in the stratosphere are likely to be dominated by internal gravity waves and therefore this type of analysis provides information on gravity wave characteristics in this region; second, comparisons between different instruments for validation purposes, such as radiosonde and satellite intercomparisons, require some measure of the geophysical variability associated with temporal and spatial variations to be able to determine coincidence criteria that will allow instrumental biases and uncertainties to be measured.

[3] To examine spatial variability we utilize pairs of profiles from radio occultation (RO) satellites in the COSMIC/FORMOSAT-3 constellation (referred to as COSMIC for brevity from this point forward). This methodology is partially inspired by work detailed by *Schreiner et al.* [2007] and *Anthes et al.* [2008] which used a similar technique to examine the precision of the COSMIC observations. While *Schreiner et al.* [2007] focuses on the precision of the instrument their analysis indicates that as profile pair separations increase the variability between observations is dominated by geophysical variations rather than instrumental uncertainties. To investigate temporal variability we utilize Rayleigh measurements from an Fe Boltzmann temperature lidar to derive stratospheric temperature [*Chu et al.*, 2002]. The precise high temporal resolution temperature measurements made by this instrument, along with the availability of extremely long continuous measurements (greater than 48 hours) and the deployment of this instrument for extended periods at two Antarctic sites make this an excellent data set to examine temporal variations in stratospheric temperature.

[1]Department of Physics and Astronomy, University of Canterbury, Ilam, Christchurch, New Zealand.
[2]Cooperative Institute for Research in Environmental Sciences, University of Colorado at Boulder, Boulder, Colorado, USA.
[3]Also at Department of Aerospace Engineering Sciences, University of Colorado at Boulder, Boulder, Colorado, USA.

0148-0227/10/2009JD013658

[4] A number of previous studies have examined the climatological structure of the gravity wavefield using radio occultation data from CHAMP [*Tsuda et al.*, 2000; *Baumgaertner and McDonald*, 2007; *Schmidt et al.*, 2008a] and COSMIC [*S. P. Alexander et al.*, 2008, 2009; *Horinouchi and Tsuda*, 2009; *Wang and Alexander*, 2009]. In particular, *S. P. Alexander et al.* [2008] found that the potential energy, E_p, of these waves is mostly related to the subtropical jet stream with some regional-scale contributions from orography in the region of the wavefield observed by RO satellites. However, the aim of the current study is to derive gravity wave characteristics other than the climatological structure of the gravity wave activity. Studies focused on deriving other gravity wave characteristics have used closely spaced observations from satellites. For example, *Ern et al.* [2004] used adjacent vertical temperature profiles measured by the CRISTA instrument to estimate the horizontal wavelength of gravity waves by an examination of phase variations between profiles. Their work also detailed a methodology to derive the absolute value of the momentum flux using a combination of temperature variations and derived values of the vertical and horizontal wavelength. An updated methodology for this type of analysis has also been used successfully by *M. J. Alexander et al.* [2008] to analyze HIRDLS observations. More recent work by *Horinouchi and Tsuda* [2009] has utilized the dense sampling of COSMIC observations to investigate gravity waves in the lower stratosphere. They found that the tangent points of the RO events from successive passages of the Low Earth Orbiting (LEO) satellites which make up the constellation, were frequently aligned in more or less linear shapes over periods less than an hour early in the constellation lifetime. *Horinouchi and Tsuda* [2009] exploited this feature to examine horizontal structures associated with gravity waves in the lower stratosphere. Their study suggested that the horizontal wavelengths of gravity waves in the northern middle to high latitudes are generally smaller than those in the equatorial region, as previously observed by *Ern et al.* [2004].

[5] Many studies have examined gravity waves using instruments with good temporal and vertical resolutions and thus been able to derive vertical wave number and frequency power spectra. However, only a few measurements of the horizontal wave number power spectra or the related second-order structure function [*Davis et al.*, 1994] have been made. Probably the most important analyses of the horizontal wave number power spectra have been made by aircraft and airglow techniques, but have been limited in time, latitude and altitude coverage. For example, *Nastrom and Gage* [1985] used aircraft observations to show that in the upper troposphere, spectra of potential temperature and horizontal velocity have slopes of −5/3 with respect to horizontal wave number for scales below 300–400 km and at larger scales the power law steepens to an approximately −3 slope. Limited amounts of data in the lower stratosphere have also indicated that the spectral amplitudes for potential temperature are larger than those in the troposphere [*Nastrom and Gage*, 1985; *Bacmeister et al.*, 1996]. Work by *Wu* [2001] used observations from the UARS MLS to observe horizontal wave number power spectra in the upper stratosphere to lower mesosphere (38 to 60 km) for horizontal scales between 30 and 800 km. Their analysis indicated that the horizontal wave number spectra has a mean slope of around −2, but varies between −2 and −3. *Wu* [2001] also found that the amplitude of the spectra generally grows rapidly with altitude between 38 and 61 km and exhibits less growth above that altitude. Their analysis also showed significant hemispheric differences, in particular, spectra for the Northern Hemisphere winter generally had larger amplitudes and steeper slopes in the upper stratosphere than those in the Southern Hemisphere and this pattern reversed in the Northern Hemisphere summer. Smaller latitudinal variation was also observed at the equinoxes. The amplitude growth observed was also suggested to be scale dependent in the upper stratosphere showing less efficient propagation for large-scale waves. In addition, work detailed by *Eidmann et al.* [2001] used CRISTA measurements for a 1 week period in August 1997 to derive horizontal wave number spectra at 30 km altitude. Their work found temperature spectra with slopes between −5/3 and −2 for horizontal scales between 256 and 1024 km. The use of COSMIC observations between 15 and 35 km in our current study provides measures of the horizontal variability at these scales in this altitude range for different seasons for the first time.

[6] In addition, a small number of studies have examined spatial and temporal variability using paired observations to quantify variability for validation studies [*Kitchen*, 1989; *Sofieva et al.*, 2008]. *Kitchen* [1989] gathered statistics on atmospheric variations on scales from a few tens to several hundred kilometers and from a few hours to a few tens of hours, this analysis being accomplished by examination of routinely available radiosonde data and additional intensive radiosonde trials over the United Kingdom. Their work indicates that spatial and temporal variability in the troposphere and lower stratosphere is highest around 250 hPa (the tropopause level) for both temperature and wind speed. Their study also indicates that separations of less than a few tens of kilometers and 1 or 2 hours are necessary for comparisons between point measurement instruments and that comparisons with area measurement instruments, such as satellite radiometers, may require synchronized radiosonde launches to allow useful comparisons. More recent work by *Sofieva et al.* [2008] utilized radiosonde observations launched from Sodankyla station to examine variations in the stratosphere. Their analysis demonstrates that small-scale structures become different if the spatial separation between radiosonde measurements exceeds 20–30 km and natural variability can contribute significantly to the observed temperature differences for larger scales. This implies that profiles should be almost exactly colocated in time and space for validation of high-resolution profiles. Their analysis shows that the RMS temperature difference rapidly grows with increasing horizontal distance. In particular, for their radiosonde comparisons in the lower stratosphere the RMS temperature difference is 0.5 K at 40 km, 0.7 K at 80 km and 1–1.5 K for separations between 200–1000 km. *Sofieva et al.* [2008] also used COSMIC data of *Anthes et al.* [2008] to examine the observed variability in the Northern Hemisphere. We utilize COSMIC observations to update these analyses to a wider range of regions and different seasons.

[7] A description of the instruments and the data analysis methodologies used in this study are detailed in section 2.

Results from examination of pairs of COSMIC profiles are discussed in section 3.1 and from the Fe Boltzmann lidar observations in section 3.2. Interpretations of these results and comparisons with previous studies are then detailed in section 4. Initial conclusions and suggestions for further work are given in section 5.

2. Instruments

[8] *Liou et al.* [2007] and *Anthes et al.* [2008] provide detailed discussions of the COSMIC/FORMOSAT-3 radio occultation system and some initial results. Temperature, pressure, and humidity profiles of the Earth's atmosphere can be derived through the radio occultation technique. The RO technique is based on measurements of the bending of the signal emitted from a Global Navigation Satellite System (GNSS) satellite as this signal passes through regions of differing atmospheric refractivity. Inversion of the bending angle information provides temperature data with sub-Kelvin accuracies when both frequencies in the GPS system are used and has been shown to be of high enough quality to be used for climate studies [*Steiner et al.*, 2009]. In this study, we utilize the COSMIC level 2 "dry temperature" product produced at the University Corporation for Atmospheric Research. The level 2 'dry temperature' is derived from the refractivity by assuming hydrostatic equilibrium and neglecting the existence of water vapor in the inversion. The dry temperature can be regarded as the actual temperature in the dry upper troposphere and stratosphere where the quantity of water vapor is very small. In the UCAR retrieval, the full spectrum inversion method [*Jensen et al.*, 2003] is used in the lower part of the profiles, and the geometric optical method is used for the upper part of the profiles. The altitude at which these methods are utilized is not constant, though the change between processing methodologies usually occurs in the upper troposphere according to *Horinouchi and Tsuda* [2009].

[9] During the first few months after launch, the six LEO satellites which make up the COSMIC constellation were orbiting in close proximity and changes to these orbits were not completed until approximately a year after launch. During this period nonuniform geographical sampling produces clusters of observations which we will utilize in this study. As previously indicated, these closely spaced soundings from independent instruments and platforms have been taken advantage of to estimate the precision of the RO technique [*Schreiner et al.*, 2007] and for gravity wave studies [*Horinouchi and Tsuda*, 2009]. Statistics of the differences in refractivities for very closely spaced profile pairs detailed in *Schreiner et al.* [2007] show that the standard deviation between pairs is smallest between about 8 and 20 km altitude and the precision of refractivity data less than 0.2% in this region and degrades to 0.7% by 30 km. Their study notes that even with only a 10 km horizontal separation between profiles, there can still be significant real meteorological variability. We use a similar methodology with greater horizontal separations (25 to 1000 km) to examine this small-scale geophysical variability which was shown, but not discussed in detail in this previous work.

[10] Observations from an Fe Boltzmann temperature lidar located at the South Pole in 2000 and 2001 and at Rothera in 2003 and 2004 have also been utilized in this study. Details about the design, development and first observations from this lidar system are discussed by *Chu et al.* [2002]. A description of the observational campaigns can be found in the work of *Yamashita et al.* [2009]. This study only uses the Rayleigh returns observed between the stratospheric aerosol layer (where aerosol scattering would dominate) and below the Fe layer (where resonant scattering would occur). The purely molecular (or Rayleigh) scattering in the region is proportional to the atmospheric density, and the temperature profile can be derived from the relative atmospheric density profile by use of the Rayleigh lidar technique [*Hauchecorne and Chanin*, 1980]. This involves integrating the relative density profile downward by use of a starting temperature at the highest altitude in combination with the hydrostatic equation and the ideal gas law.

3. Results

3.1. Spatial Variability Measured by COSMIC/FORMOSAT-3

[11] Figure 1 shows the distribution of paired COSMIC profiles in January 2007 with spatial and temporal separations less than 500 km and 1 hour, respectively. The temperature differences between pairs at 25 km altitude are defined by the color of the dots. Examination of Figure 1 shows that there is a distinct hemispheric asymmetry. This hemispheric difference is most clearly observed in Western Europe and Siberia where the temperature differences are on average larger than those observed elsewhere in either hemisphere. It should also be noted that the vast majority of COSMIC profile pairs occur at midlatitudes (between 30° and 70° in both hemispheres) and far fewer pairs are observed in the equatorial region and at the poles.

[12] Figure 2 displays histograms of the number of paired observations in the specified temperature difference range for a set of different horizontal separations for January 2007. The number of paired observations increases as the horizontal separation increases, reflecting the fact that it becomes increasingly unlikely to observe a pair of profiles as the horizontal separation becomes small. Inspection also suggests that in all horizontal separation ranges the distributions' tails occur more often than in the Gaussian distribution. The kurtosis for Figures 2a–2d range from 6.7 to 11.8, while the kurtosis for a Gaussian distribution is 3 [*Barlow*, 1989]. The definition of kurtosis may be written as

$$\text{Kurtosis}(x) = \frac{\sum_{n=1}^{N}(x_n - \bar{x})^4}{N\sigma^4}, \tag{1}$$

where $\bar{x}$ and σ are the mean and standard deviation of the values x_1 to x_N, respectively. The kurtosis measures the relative peakedness or flatness of a distribution. In particular, values of kurtosis greater than 3 result when a distribution with a higher peak or wider tails than the Gaussian distribution with the same mean and standard deviation occur. In this case, the values of kurtosis greater than 3 are related to distributions with wider tails than the equivalent Gaussian distribution.

[13] Interestingly, by examining differences in trace gas characteristics as a function of horizontal separation to derive spatial variability information for satellite validation,

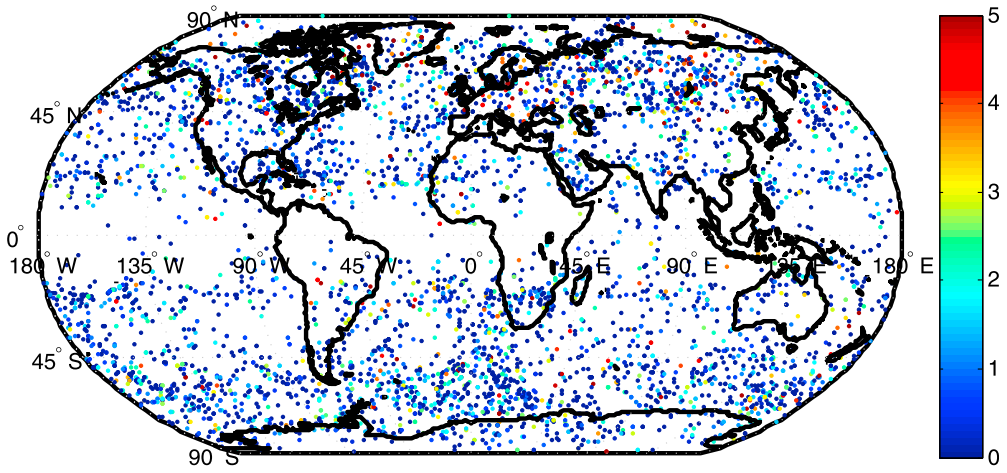

Figure 1. Scatterplot displaying the geographic position and the temperature difference (color of dots) between pairs of COSMIC observations in January 2007 at 25 km altitude. The pairs displayed have been selected based on the spatial and temporal separations between the profiles being less than 500 km and 1 hour, respectively.

Sparling et al. [2006] also observed long-tailed distributions which they believed to be due to the advection of different air masses. Thus, this pattern seems likely to be representative. Comparison of Figures 2a–2d shows that the range of temperature differences observed increases as a function of horizontal separation. For example, the range of temperature differences for horizontal separations of 0–250 km shown in Figure 2a is approximately half the range observed for horizontal separations of 750–1000 km displayed in Figure 2d based on the standard deviation, σ.

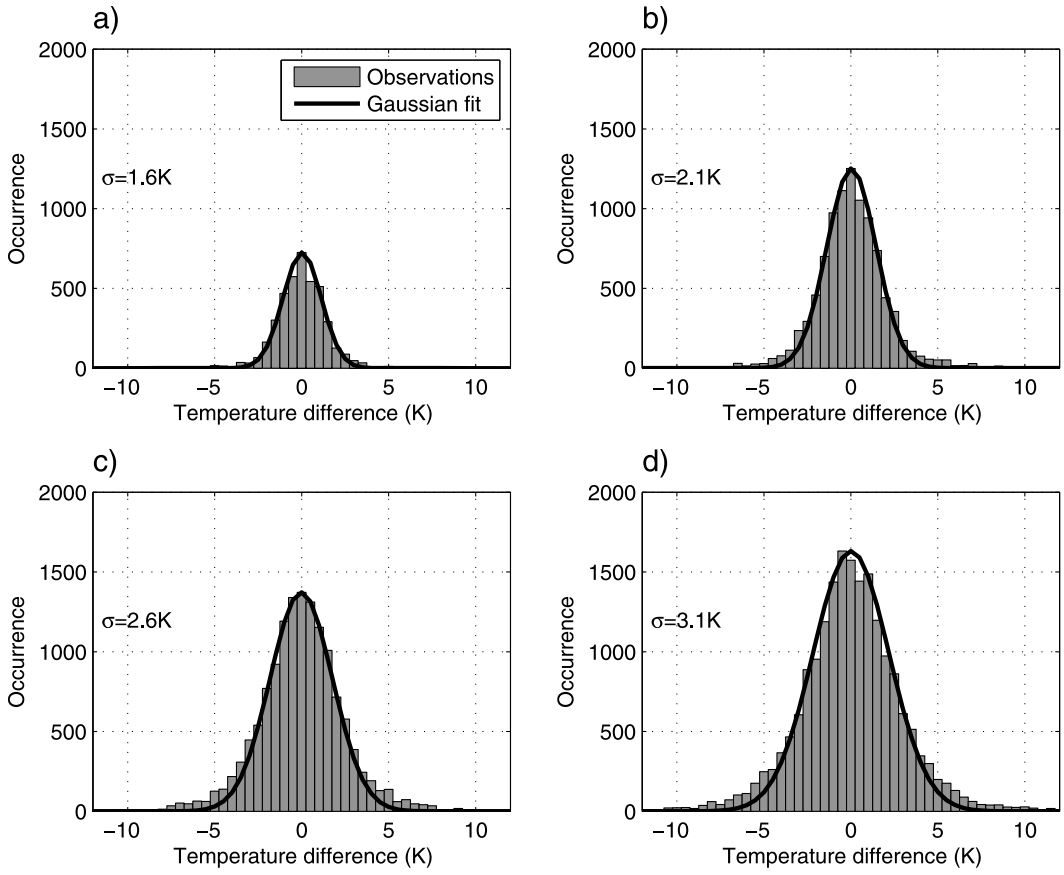

Figure 2. Histograms of the number of observations within a specified temperature difference range for horizontal separations between (a) 0 and 250 km, (b) 250 and 500 km, (c) 500 and 750 km, and (d) 750 and 1000 km. Also displayed are Gaussian fits to the data.

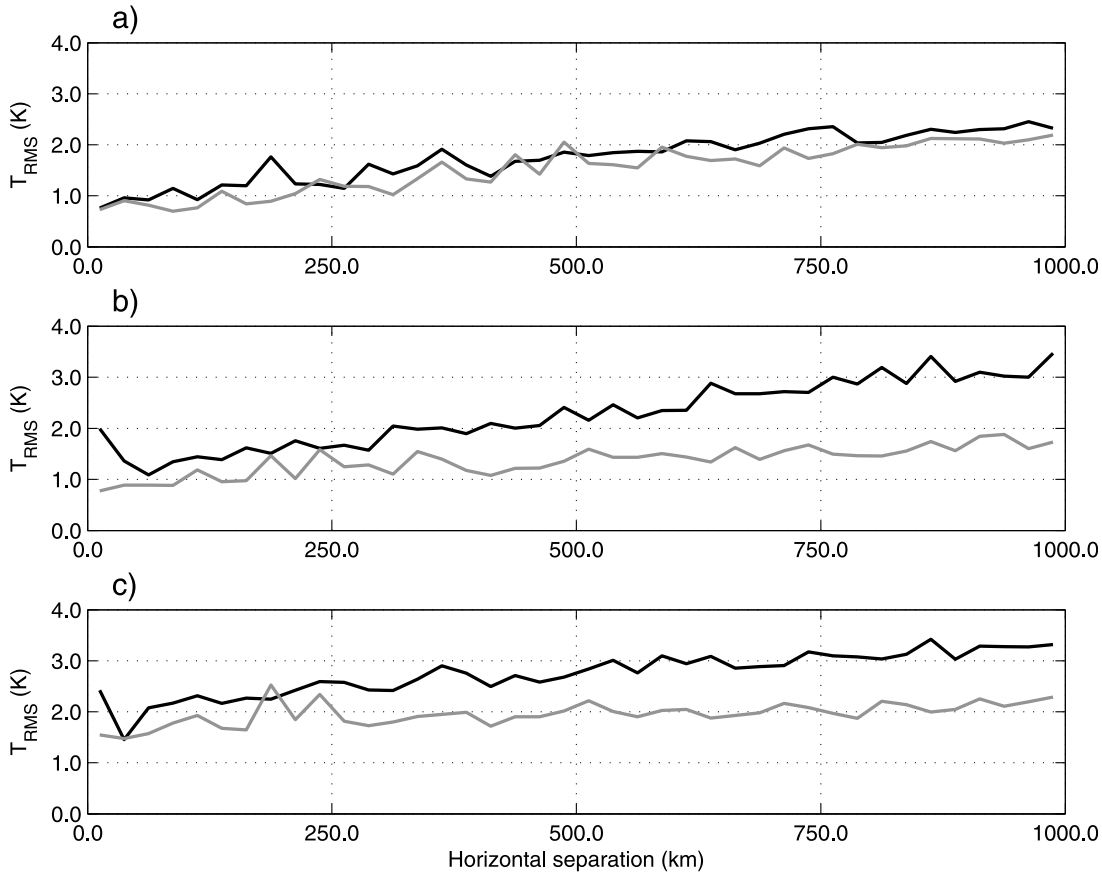

Figure 3. Spatial separation versus RMS temperature difference (T_{RMS}) between pairs of COSMIC profiles observed in January 2007 that are separated in time by no more than 1 hour for altitudes of (a) 15, (b) 25, and (c) 35 km. The solid line represents the Northern Hemisphere results, and the shaded line represents the Southern Hemisphere results.

[14] To further examine this pattern, Figure 3 shows the spatial separation versus RMS temperature difference (T_{RMS}) derived from pairs of COSMIC data from January 2007 averaged over the Northern and Southern Hemispheres for a number of altitudes. The T_{RMS} can be written as

$$T_{RMS}(h) = \sqrt{\langle [T(x+h) - T(x)]^2 \rangle}, \quad (2)$$

where $T(x)$ is the temperature at position x derived from a COSMIC profile and $T(x + h)$ is the temperature at position $x + h$ derived from the other COSMIC profile in the pair, h is the horizontal separation between the two profiles and the triangular brackets indicate an ensemble average (which in this case is associated with ranges of horizontal separations). Before calculating the T_{RMS} at a particular altitude a linear trend is removed from the temperature difference profile created from the COSMIC profiles (examined over the 15 to 35 km altitude range) which make up the pair. This trend removal reduces variations in the T_{RMS} pattern associated with large-scale background changes and planetary-scale wave variations which would have vertical scales greater than 20 km. However, it should be noted that recent studies have shown a significant amount of gravity wave activity associated with vertical wavelengths close to and greater than 20 km, for example [*Alexander and Barnet*, 2007]. The RMS temperature differences are then calculated from all the observations within a 25 km horizontal separation bin which is incremented by 25 km steps to cover the 25 to 1000 km horizontal separation range. The horizontal separations displayed are not defined in any direction and thus temperature differences associated with both zonal and meridional variations are included in these values. Figure 3 shows that in both hemispheres the T_{RMS} increases almost linearly with horizontal separation at all altitudes. At the smallest separations, T_{RMS} increases with altitude in both hemispheres. However, at larger separations (greater than 500 km) the values of T_{RMS} remain nearly constant or reduce slightly with altitude in both hemispheres. The rate of increase in T_{RMS} as a function of horizontal separation also varies as a function of altitude. The gradient derived from a linear least squares straight line fit to the data in the Northern Hemisphere is 0.15, 0.20 and 0.13 K/100 km for altitudes of 15, 25 and 35 km and 0.15, 0.08 and 0.04 K/100 km for the Southern Hemisphere, respectively. If we take the sum of the area beneath the curves as an integrated measure of the horizontal spatial variability the value increases as a function of altitude in the Northern Hemisphere and decreases from 15 to 25 km and then increases above this altitude in the Southern Hemisphere.

[15] In order to interpret these results it is important to realize that a range of processes in the atmosphere could

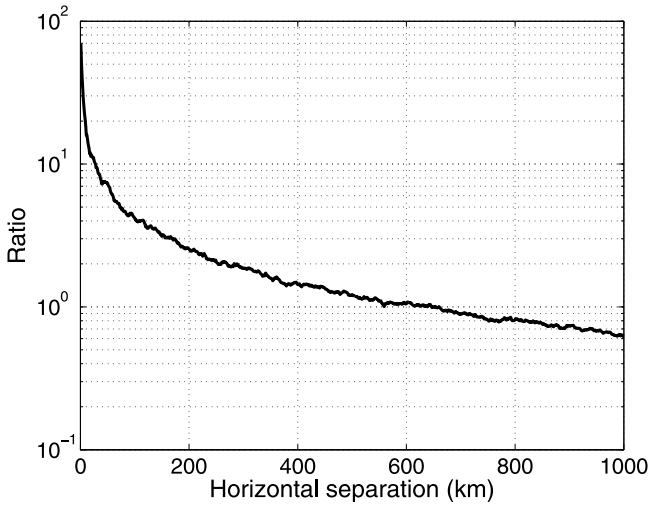

Figure 4. Ratio of the mean temperature difference derived from simulated gravity wave and planetary wavefields for differences derived between observations separated horizontally. Both means are derived from 200 independent realizations.

contribute to the temperature differences observed at a particular horizontal separation. The dominant variations are likely to be changes in the background zonal mean and variations due to planetary and gravity wave motions in the atmosphere. The linear detrending previously mentioned will remove variations with vertical wavelengths greater than 20 km. Thus, changes in the background temperature and planetary wavefield will be reduced relative to motions with smaller vertical scales, but some variability associated with internal gravity waves is also likely to be removed [*Alexander and Barnet*, 2007]. If we think about the properties of the wavefield observed, it is obvious that a set of waves with a range of horizontal wavelengths will contribute to the T_{RMS} observed at a particular horizontal separation. It is also clear that as the horizontal wavelength of a particular wave becomes large compared to the horizontal separation between the pair of profiles, the waves' contribution to the temperature difference reduces. Thus, the calculation of the temperature difference between closely spaced profile pairs acts to suppress the background mean and perturbations associated with large-scale motions, namely planetary waves. If we assume that fluctuations associated with a specific wave will be small, if the horizontal separation, h, is related to two points on a wave with a phase difference less than $\pi/4$, then the largest horizontal wavelength that will contribute to T_{RMS} will be approximately 8 hours. For a horizontal separation of 500 km waves with horizontal wavelengths less than 4000 km will therefore contribute to the T_{RMS}. Given that our sampling of pairs is strongly biased to midlatitudes (as shown in Figure 1) this procedure would suppress the contribution of planetary-scale waves with zonal wave numbers 0 to 6 for horizontal separations in the zonal direction. Interestingly, this corresponds to the range of scales removed in recent studies by *S. P. Alexander et al.* [2008] and *Wang and Alexander* [2009] which examine the gravity wavefield with COSMIC measurements.

[16] To quantitatively determine the relative contribution of the gravity wave and planetary wavefields on the temperature differences observed at two horizontally separated locations we have performed a simple Monte Carlo simulation. Our model first simulates a gravity wavefield with a horizontal power spectrum with a spectral slope of −5/3 for horizontal wavelengths between 1 and 2000 km, this upper limit being a good representative value for midlatitudes [*Preusse et al.*, 2006]. This spectrum is scaled such that the wave amplitude of the longest horizontal wavelength component in the spectrum has an amplitude of 1 K selected to be representative from values of *Alexander et al.* [2009]. We then apply an inverse Fourier transform to produce a series of values as a function of horizontal separation around a specific latitude circle. The resultant data series is formed using sets of random phases and 200 realizations are created. The temperature differences between points associated with a particular horizontal separation are calculated and the mean derived. In a similar manner, 200 realizations of a zonal wave number 1 to six stationary planetary wavefield with fixed amplitudes of 8.0, 2.0, 0.5, 0.5, 0.5 and 0.5 K, respectively, and randomized phases are produced. Note that the values for stationary planetary wave 1 to 3 are based on the largest monthly averages derived from TIMED/SABER data at midlatitudes and for the altitude region of interest [*Xiao et al.*, 2009] and thus represent close to a worst case scenario and that the latitudinal mean has not been included because the difference would obviously remove this term. The 200 realizations of the planetary wavefield are then used to derive the mean temperature difference as a function of horizontal separation.

[17] Figure 4 displays the ratio of the mean temperature differences calculated from the simulated gravity wave and planetary wavefields as a function of horizontal separation. Examination of Figure 4 shows that at short horizontal separations the temperature differences associated with the gravity wavefield are as much as 100 times larger than the temperature differences associated with the planetary wavefield. This ratio decreases rapidly for larger horizontal separations and for horizontal separations from 500 km the temperature differences associated with the gravity wave and planetary wavefields are comparable. This simple model therefore supports our suggestion that for horizontal separations less than 500 km the T_{RMS} metric would be dominated by the gravity wavefield. Given our conservative estimates of the relative amplitudes of gravity waves we can be very confident that the T_{RMS} metric provides information on gravity waves for horizontal separations less than 500 km. This is particularly true when we account for the vertical detrending applied, which would preferentially suppress planetary waves, and the fact that the planetary wave related variations would be very small when the pairs are orientated meridionally rather than zonally.

[18] The variations in altitude observed in Figure 3 are thus likely to be dominated by gravity waves which implies that either observational [*Alexander*, 1998] or critical filtering effects impact the wavefield strongly between 15 and 25 km in the Southern Hemisphere summer. To test the impact of vertical detrending, Figure 5 displays the T_{RMS} versus horizontal separation for the data with (Figure 3a) and without detrending (Figure 3b) and the ratio of the two (Figure 3c) for temperature differences at 15 km observed in

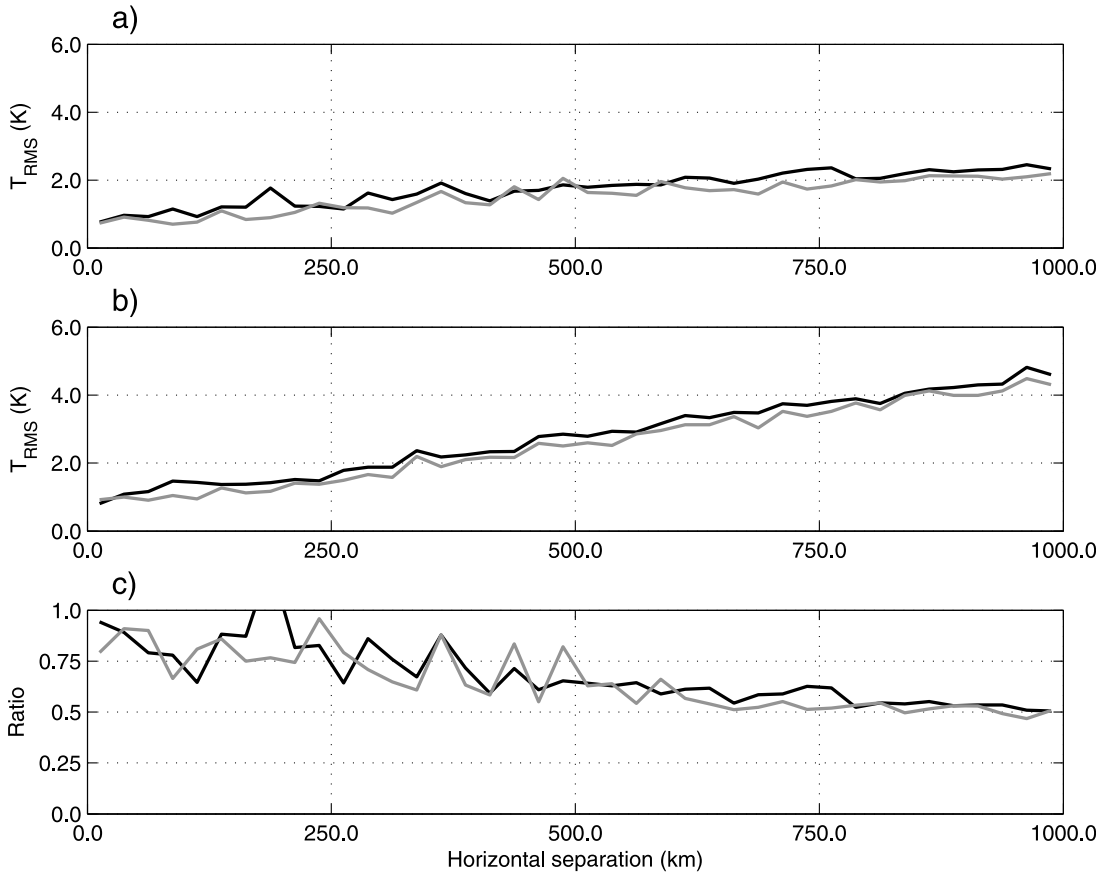

Figure 5. Spatial separation versus RMS temperature difference (T_{RMS}) between pairs of COSMIC profiles observed in January 2007 that are separated in time by no more than 1 hour for altitudes of 15 km (a) with vertical detrending of the temperature differences, (b) without detrending, and (c) the ratio of the detrended to the not detrended data. The solid line represents the Northern Hemisphere results, and the shaded line represents the Southern Hemisphere results. Note that Figure 5a is identical to Figure 3a.

January 2007. Comparison of Figures 5a and 5b shows that the T_{RMS} observed are significantly larger at large horizontal separations for the data which was not detrended. T_{RMS} values with and without detrending are more similar at shorter horizontal separations (less than 500 km). This pattern is very clear when we inspect Figure 5c which shows the ratio of the analysis with and without vertical detrending. In particular, Figure 5c shows that at short horizontal separations the ratio is close to 1 and at horizontal separations near 1000 km is close to 0.5. If we interpret the analysis with and without the vertical detrending as displaying the variations solely due to internal gravity waves and a combination of variations due to all potential processes, then Figure 5c suggests that short vertical wavelength internal gravity waves make up between 60% and 90% of the variations observed below 500 km. We will use vertical detrending on all the temperature difference profiles used from this point forward because we are particularly interested in the role of gravity waves. In addition, this analysis is more consistent with analyses such as those detailed by *Wu* [2001], who detrended horizontal radiance measurements from MLS to examine horizontal wave number power spectra which we will use for comparison purposes later in section 4.

3.1.1. Second-Order Structure Functions

[19] The information displayed in Figure 3 can be displayed in an alternative manner by deriving the structure function associated with the temperature difference data. The second-order structure function, S_2, can be written as

$$S_2(h) = \langle [T(x+h) - T(x)]^2 \rangle, \tag{3}$$

where the symbols have the same meaning as those in equation (2). A detailed discussion of structure functions is given by *Davis et al.* [1994] and recent work by *Lu and Koch* [2008] has used both spectral and structure function analysis of horizontal wind fields from aircraft data to identify scale interactions between turbulence and gravity waves. We use the fact that the scaling value of second-order structure functions can be related to the spectral slope of the power spectra via the Wiener-Khinchine theorem [*Davis et al.*, 1994; *Cho et al.*, 2000; *Eidmann et al.*, 2002]. We can therefore use our paired observational analyses to examine the form of second-order structure functions and compare these with previous results on the spectral form of the horizontal wave number spectra, such as those reported by *Nastrom and Gage* [1985] and *Wu* [2001]. In addition, work by *Kahn and Teixeira* [2009] has recently completed

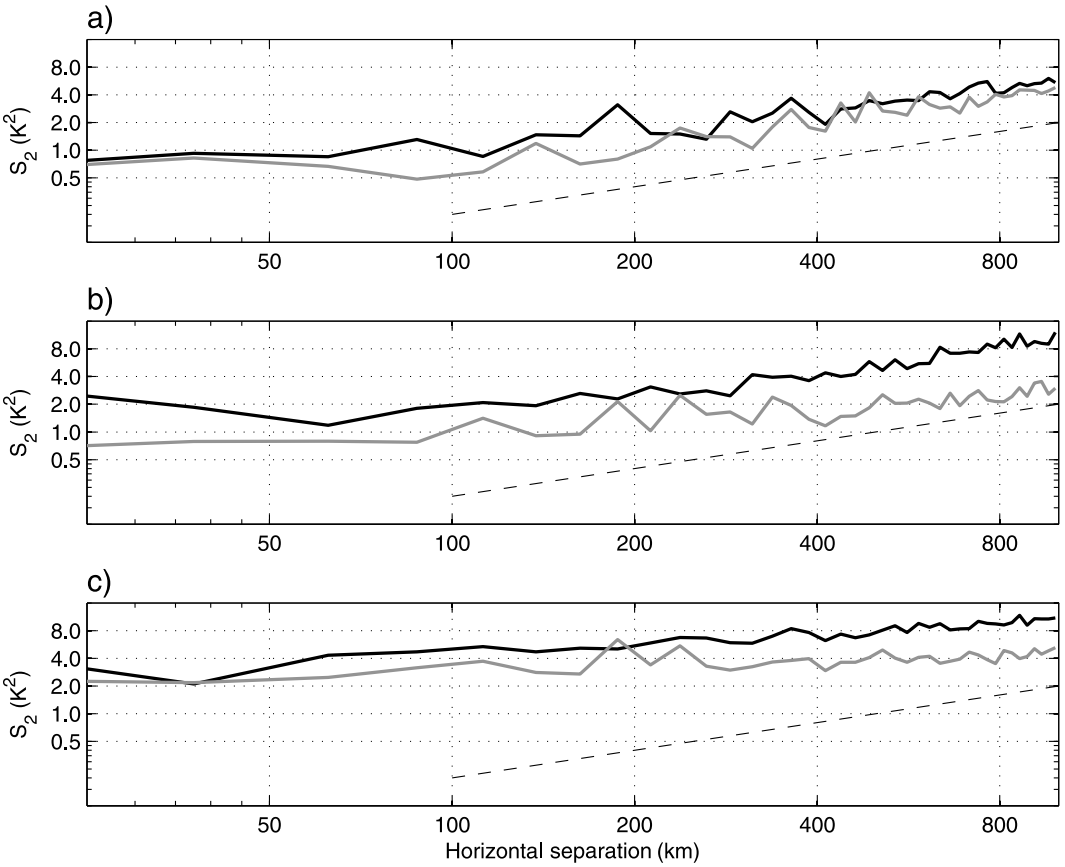

Figure 6. Horizontal separation versus the second-order structure function derived from pairs of COSMIC profiles observed in January 2007 that are separated in time by no more than 1 hour for altitudes of (a) 15, (b) 25, and (c) 35 km. The solid line represents the Northern Hemisphere results, and the shaded line represents the Southern Hemisphere results. Also displayed by the dashed line is a reference h^1 scaling.

some similar analysis using the scaling properties of temperature variance in the troposphere derived from AIRS observations.

[20] Figure 6a shows the second-order structure function at 15 km for January 2007. The lines for both the Northern and Southern Hemispheres approximate straight lines between 100 and 1000 km with slopes of 0.9 and 0.8, respectively. These gradients are therefore similar to the reference h^1 line displayed in Figure 6. Previous studies, such as *Cho et al.* [2000] and *Lu and Koch* [2008] indicate that this h^1 scaling is consistent with a horizontal wave number power spectra with a k^{-2} spectral slope, where k is the horizontal wave number.

[21] Figure 6b displays the second-order structure function derived from pairs of observations in January 2007 at an altitude of 25 km. The second-order structure functions have a constant gradient for horizontal separations greater than 100 km. However, in this case the gradients are somewhat shallower than the h^1 reference slope with values of 0.8 and 0.4 in the Northern and Southern Hemispheres, respectively. Another difference between the patterns displayed in Figures 6b and 6a is that the S_2 values in the Northern Hemisphere are always greater than those in the Southern Hemisphere for the same horizontal separation in Figure 6b. Figure 6c shows an extension of the changes observed between Figures 6a and 6b, namely structure functions with shallower slopes at the higher altitude of 35 km are observed and a separation in the values between the Northern and Southern Hemispheres remains clear. It should be noted that using values of the precision of the COSMIC data, conservatively 0.5 K between 8 and 20 km [*Anthes et al.*, 2008], suggests that the measurement noise level (0.25 K^2) are well below the values observed at even the smallest horizontal separations and thus do not substantially contribute to the patterns observed. It is also relevant to indicate at this point that use of the mid-frequency approximation of the gravity wave dispersion relation shows that at small horizontal separations (100 km) the variability will be more strongly affected by the temporal differences between profile pairs than at other horizontal separations. Thus, the signals below 100 km horizontal separations may be significantly affected by intermittency and temporal variations in the wavefield.

[22] Second-order structure functions derived from pairs of COSMIC temperature profiles observed in July 2007 for a range of altitudes are displayed in Figure 7. At the lowest altitude (15 km) displayed in Figure 7a the pattern observed is very similar to that in Figure 6a. In particular, the gradients are very similar, 0.9 in both cases over the horizontal separation range 100–1000 km, and values at particular

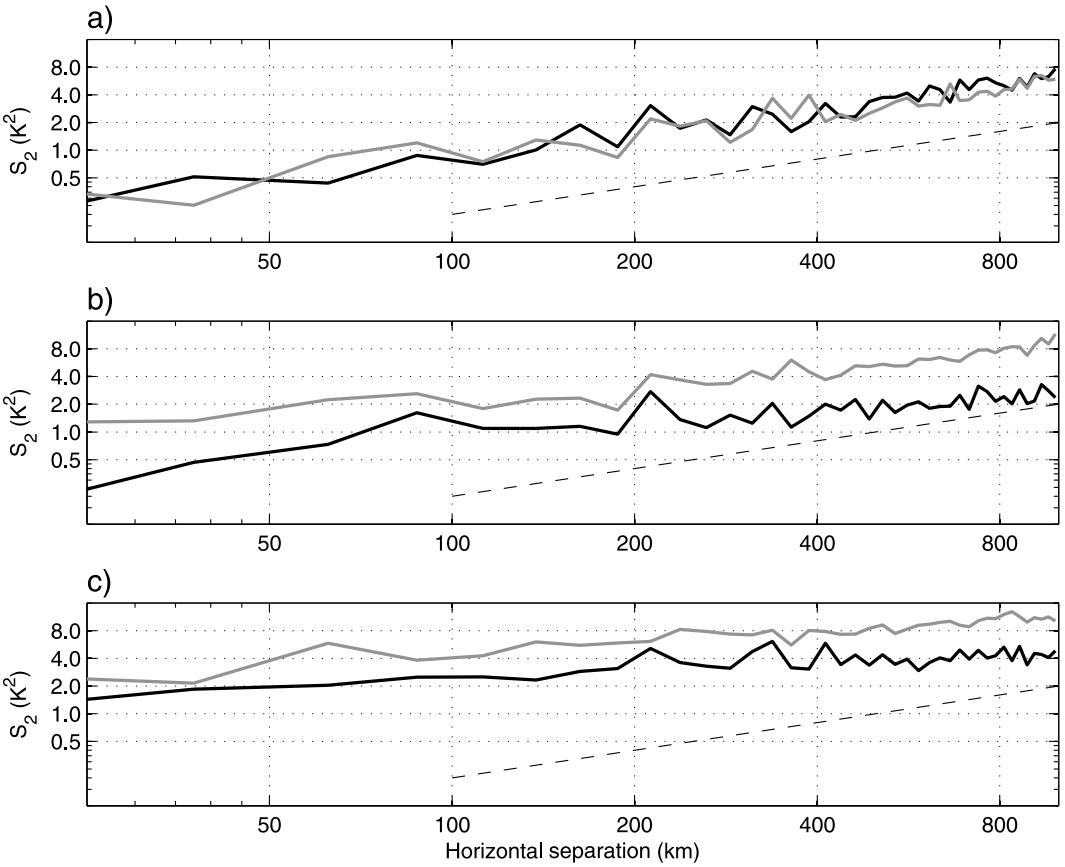

Figure 7. As in Figure 6, but for July 2007.

horizontal separations for the Northern and Southern Hemisphere are nearly identical. Comparison of Figures 7a and 7b shows that the gradients of the second-order structure function reduce to 0.4 and 0.75 for the Northern and Southern Hemisphere, respectively, from 15 to 25 km altitude. The gradients also reduce further with increasing altitude (see Figure 7c). The values of the second-order structure function are also larger in the Southern Hemisphere than the Northern Hemisphere at all horizontal separations at the two higher altitudes displayed. This is a reversal of the pattern observed in Northern Hemisphere winter (see Figures 6a and 6b) and corresponds with the patterns observed in horizontal wave number spectra at higher altitudes previously detailed by *Wu* [2001]. The range of spectral slopes also matches the values identified by *Eidmann et al.* [2001].

3.1.2. Altitudinal and Geographical Variations in T_{RMS}

[23] The variation in T_{RMS} as a function of altitude is shown in Figure 8 for the Northern (Figure 8a) and Southern Hemisphere (Figure 8b) for July 2007 measurements. The enhancement observed in Figures 8a and 8b between 15 and 20 km could be due to the strong latitudinal temperature gradients associated with the tropical tropopause. Another possibility is strong variations in the gravity wave activity as observed in this region by *S. P. Alexander et al.* [2008] using COSMIC observations.

[24] Examination of Figure 8 also suggests that difference between the various horizontal separations as a function of altitude provide information about gravity waves and their relative propagation characteristics. In particular, the values of T_{RMS} for different horizontal separations get closer together as altitude increases in the Northern Hemisphere. While in the Southern Hemisphere the T_{RMS} differences between lines associated with different ranges of horizontal separation remain similar until approximately 25 km. At this point the rate of increase of individual horizontal separation ranges starts to vary with the values of T_{RMS} at large horizontal separations displaying a slower increase as a function of altitude than smaller horizontal separations.

[25] Figure 9 shows the geographic variation of the T_{RMS} derived from pairs of COSMIC data for July 2007 at an altitude of 15 km. Note that the ensemble averages used to derive T_{RMS} are now calculated in 10 degree latitude and 30 degree longitude bins, and values are only plotted in bins which contain more than 100 pairs. In this case we have only determined the T_{RMS} for pairs of observations that have horizontal separations less than or equal to 500 km and thus these patterns are likely to be dominated by variations in the gravity wave activity based on our previous reasoning. High values of T_{RMS} are observed toward the equator which correspond well with the patterns observed by *Tsuda et al.* [2000] and *S. P. Alexander et al.* [2008], among others. These latitudinal patterns in wave activity have previously been explained by *Alexander et al.* [2002] as being associated with the latitudinal variation of the Coriolis parameter which acts to increase the allowable range of frequencies of

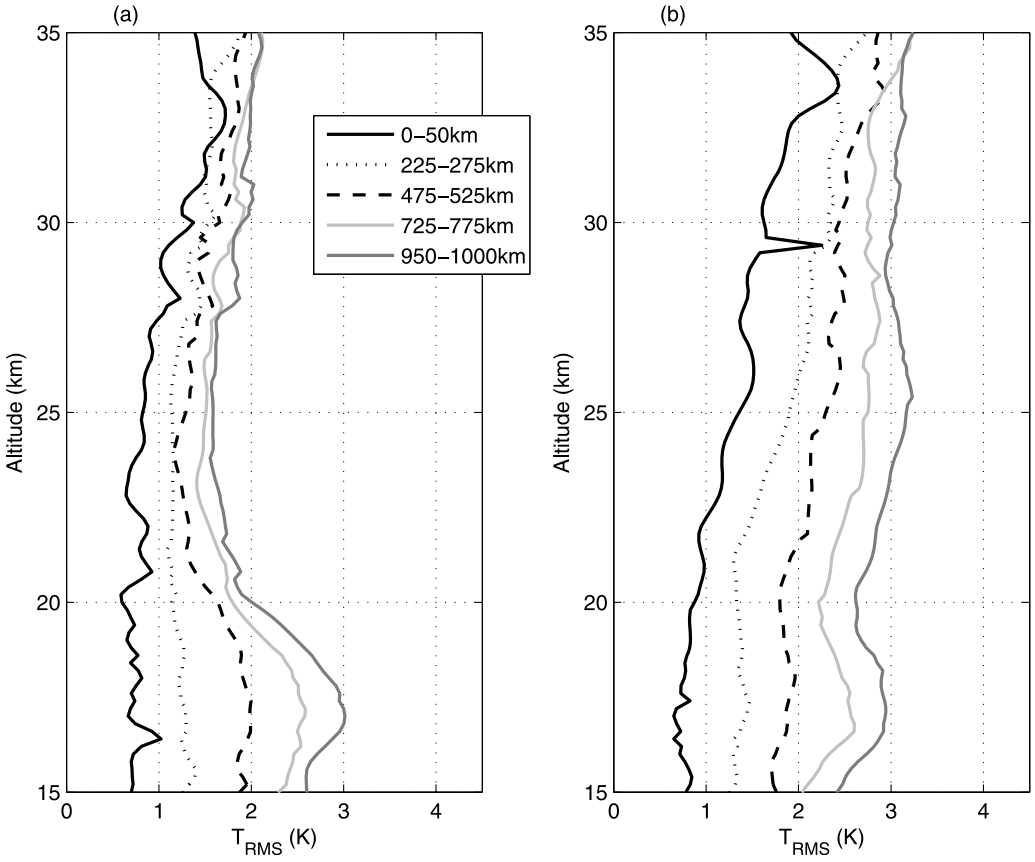

Figure 8. T_{RMS} between pairs of COSMIC profiles separated by the distances identified in the legend as a function of altitude for (a) Northern and (b) Southern Hemisphere observations made in July 2007.

waves toward the equator, which will be discussed more fully in section 4. However, this pattern could also be partially related to variations in the structure of the tropopause level in this region [*Schmidt et al.*, 2008b] or potentially large amplitude high wave number planetary waves could also potentially explain this pattern. Close inspection of Figure 9 also shows enhancements in the Northern Hemisphere subtropics in the vicinity of the Gulf of Mexico and

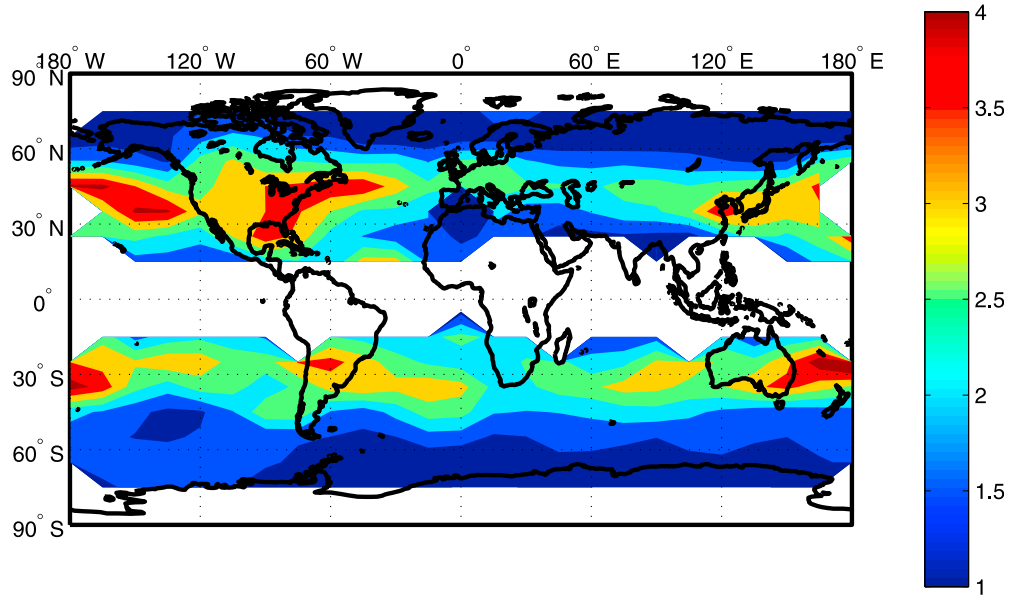

Figure 9. RMS temperature difference at 15 km between pairs of COSMIC profiles less than 500 km and 1 hour apart as a function of geographic position for observations made in July 2007.

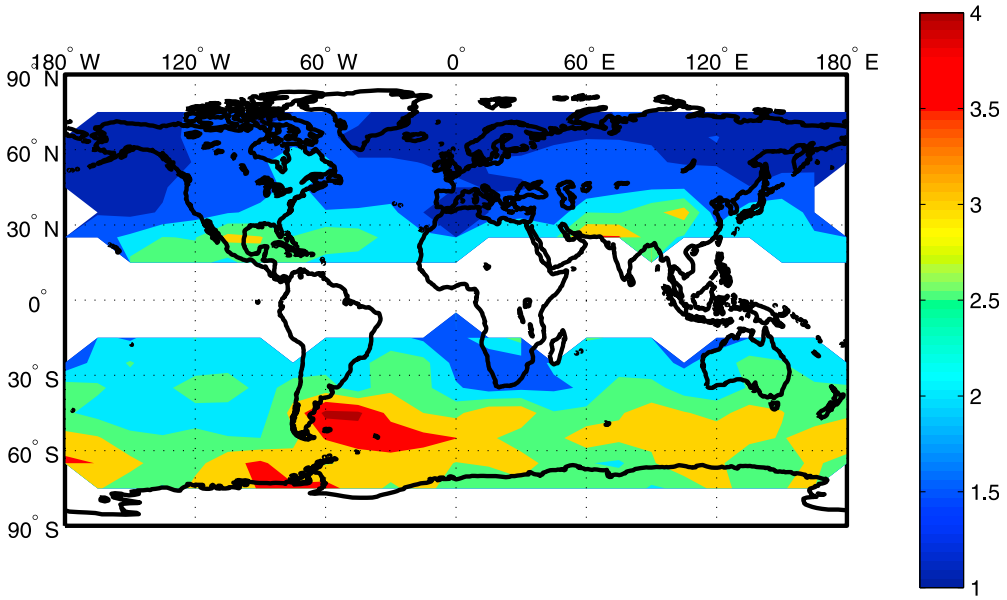

Figure 10. As in Figure 9, but for 30 km altitude.

the Kuro-shiro stream, regions which have previously been identified as regions of strong gravity wave activity associated with convection [*Preusse et al.*, 2001; *Jiang et al.*, 2004; *Preusse and Ern*, 2005]. Examination of the geographic distribution of horizontal separations (not shown) indicates that these patterns are not associated with sampling issues.

[26] The geographic variation of T_{RMS} derived from pairs of COSMIC data for July 2007 at an altitude of 30 km is displayed in Figure 10. In this case, high values of T_{RMS} are not symmetric around the equator and large values of T_{RMS} are predominantly observed in Southern Hemisphere high latitudes. Figure 10 also shows a good deal of longitudinal structure in the winter hemisphere with a clear enhancement near the Antarctic peninsula and the tip of South America. Figure 10 also displays enhancements in the vicinity of the Gulf of Mexico and the Kuro-Shiro stream.

3.2. Temporal Variability Measured by Lidar

[27] Figure 11 shows the time difference versus T_{RMS} derived from a ground-based Fe Boltzmann temperature lidar at 40–42 km, which was located at South Pole between 2000 and 2001 and at Rothera (67°S, 68°W) in 2003 and 2004. The longest high-quality data sets were used to derive the ensemble mean for the different time lags displayed in Figure 11 using a time integration of 30 minutes and an altitude resolution of 2 km for both sites. It should be noted that the South Pole observations were dominated by measurements made in the Southern Hemisphere summer, while the Rothera data selected was more evenly distributed through the year. We use these measurements because we can ignore effects associated with spatial separation in this data since all measurements are colocated. However, the limited number of lidar observations means that it is not possible to calculate the RMS temperature difference at a seasonal scale accurately. But, given the seasonal variations identified by *Yamashita et al.* [2009] this may be a potential limitation of this analysis.

[28] Examination of the variation in the Rothera data (solid line in Figure 11) displays a steady increase in T_{RMS} until time separations of approximately 5–6 hours and an asymptotic variation after 6 hours. *Sparling et al.* [2006] points out that the change to a constant as a function of spatial separation identifies the correlation length in tracer data. Thus, in a similar manner we can identify the correlation time of stratospheric temperatures to be 6 hours from Figure 11 for Rothera. Note that the relatively large value of T_{RMS} at small time differences could be associated with instrumental effects or could be related to the position of the instrument near the Antarctic peninsula, a known gravity wave 'hot spot' (see Figure 10). Examination of the variation in the South Pole data (dotted line in Figure 11) shows an increase as a function of increasing time difference with

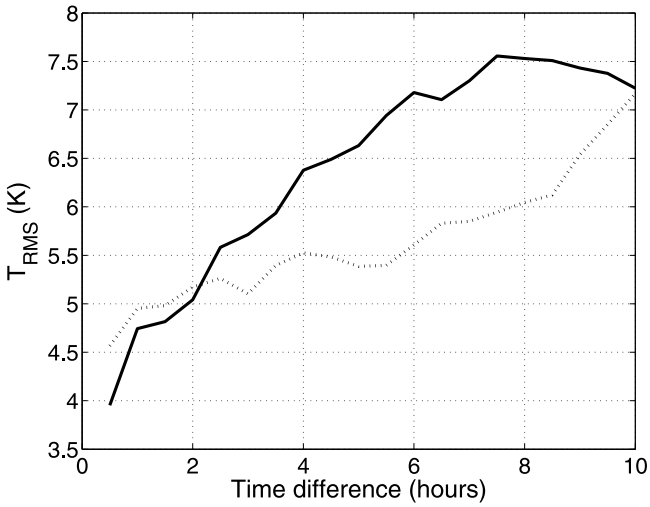

Figure 11. Temporal separation versus RMS temperature difference derived from Rayleigh measurements from Rothera (solid line) and the South Pole (dotted line).

some signs of a flattening of the T_{RMS} change at time greater than 5 hours. Comparison also indicates that the area under the T_{RMS} curve for the South pole is significantly less than that observed for Rothera. If we assume this area represents the variations due to gravity waves then this difference suggests less gravity wave activity at the South Pole than Rothera which is supported by work detailed by *Yamashita et al.* [2009]. Analysis of superpressure balloon observations from the Vorcore campaign also display this pattern [*Vincent et al.*, 2007; *Hertzog et al.*, 2008]. In particular, *Yamashita et al.* [2009] noted enhanced gravity wave activity in the Southern Hemisphere winter at Rothera compared to observations at the South Pole. This also implies that the slightly larger value of T_{RMS} at small time differences observed at the South Pole compared to Rothera is associated with differences in the signal-to-noise ratio due to the South Pole observations being made during daylight conditions predominantly. Though it should be noted that the uncertainty associated with individual measurements (associated with photon noise) are such that they can only explain values of T_{RMS} of approximately 3 K and thus even at short time lags the temperature differences are impacted by geophysical variability.

4. Discussion

[29] The results described in section 3.1 are very suggestive that the spatial variability displayed is dominated by variations associated with internal gravity waves. In particular, the geographical variability of the T_{RMS} in Figure 10 exhibits clear localized enhancements near the Antarctic peninsula and the tip of South America which have both been highlighted as regions of high gravity wave activity in previous studies [*Eckermann and Preusse*, 1999; *Wu and Jiang*, 2002; *Alexander and Barnet*, 2007; *Baumgaertner and McDonald*, 2007; *Alexander et al.*, 2009]. Similar localized enhancements are also observed in the Northern Hemisphere subtropics near the Gulf of Mexico and the Kuro-Shiro stream, both of which having been linked to regions of strong wave activity related to convective sources [*Preusse et al.*, 2001; *Jiang et al.*, 2004; *Preusse and Ern*, 2005]. The prominent latitudinal variation observed (see Figure 9) also corresponds with patterns previously identified in gravity wave activity climatologies. Thus, the paired observation methodology detailed in this study is likely to provide us with an alternative way to examine the internal gravity wavefield.

[30] The second-order structure functions displayed in Figure 6 and Figure 7 offer the potential to examine the wavefield in a manner which can highlight variations at different horizontal separations which in turn can be related to the horizontal wave number power spectra [*Lu and Koch*, 2008]. Given the sparsity of measurements of the horizontal wave number power spectra or the equivalent second-order structure function this is important. Inspection of the observed scaling values in the lower stratosphere in Figure 6a and Figure 7a show remarkably similar patterns for horizontal scales greater than 100 km and little or no hemispheric differences which seems to be at odds with observations at higher altitudes detailed by *Wu* [2001]. Conversely, the observed scaling slopes near 1, which correspond to a power spectra slope of −2, compare relatively well with values in the 100 to 400 km range detailed by *Nastrom and Gage* [1985] and the values of *Wu* [2001] and *Eidmann et al.* [2001]. Changes in the spectral slope at larger horizontal scales (above 400 km) toward a k^{-3} scaling indicated by *Nastrom and Gage* [1985] are not observed. In this aspect, the present results correspond more closely to those of *Wu* [2001] and *Lovejoy et al.* [2009] which did not observe a scale break. These observations therefore potentially support the interpretation of *Lovejoy et al.* [2009] that the effect of turbulence on aircraft observations could lead to spurious breaks in the scaling and to the spurious appearance of the vertical scaling exponent at large horizontal lags.

[31] Examination of higher-altitude observations (see Figures 6b and 6c and Figures 7b and 7c) shows clear hemispheric differences with larger values of the second-order structure function observed in the winter hemisphere. *Wu* [2001] found that spectra observed in the winter in the Northern Hemisphere generally had larger amplitudes and steeper slopes in the upper stratosphere than those in the Southern Hemisphere summer and also indicated that this pattern reversed for the Northern Hemisphere summer. The results of our analysis thus show a matching seasonal pattern in the altitude region between 25 and 35 km and smaller hemispheric differences in the lower stratosphere. The most obvious explanation for this difference seems to be critical level filtering associated with the different seasonal structure of the zonal wind patterns observed between 15 and 25 km. The background zonal winds in this region display prevailing eastward winds in the winter and westward winds in the summer, while at lower altitudes the winds remain predominantly eastward. Thus, in the Southern Hemisphere summer (displayed in Figure 6) internal gravity waves propagating from regions below the tropospheric jet with small eastward and westward phase velocities would be removed from the wavefield due to critical level filtering in this region. Importantly, orographic waves with zero phase velocity would also be removed from the spectrum in this region. Note that comparisons between SABER observations and results from the GROGRAT ray tracing model detailed by *Preusse et al.* [2008] have previously indicated that the wind reversal between tropospheric westerlies and stratospheric easterlies in summer strongly contributes to the critical-level filtering of slow phase-speed waves. In the Northern Hemisphere winter only the waves with small westward phase velocities would be removed from the wavefield in this region. Similar arguments can be made for the Southern Hemisphere winter and Northern Hemisphere summer. Previous work detailed by *S. P. Alexander et al.* [2008] has indicated that strong wave filtering above the jet stream core results in decreases of E_p around the 0–10 ms^{-1} zonal velocity line, suggesting low ground-based phase speeds of these waves which interact with the background wind. Analysis detailed by *Baumgaertner and McDonald* [2007] has also highlighted the potential for critical level filtering of orographic waves being a major contributing factor to the seasonal pattern observed over Antarctica and particularly the Peninsula region. Enhancements in Figures 9 and 10 in the vicinity of the Gulf of Mexico and Kuro-Shiro stream which are related to convective sources with large phase speeds also indicates that filtering may be most effective on waves with low phase velocities.

[32] Figure 8 shows that larger horizontal separation ranges display less growth in T_{RMS} as a function of altitude than shorter horizontal separation ranges between altitudes of 20 and 35 km in the Northern Hemisphere. This perhaps indicates that larger horizontal wavelength gravity waves are removed preferentially from the wavefield in this region in the summer. Examination of Figure 8b also shows that above 25 km the larger horizontal separation ranges show less growth in T_{RMS} as a function of altitude than shorter horizontal separation ranges which again indicates that large horizontal wavelength waves are preferentially removed from the wavefield. Thus, our analysis suggests preferential filtering of larger horizontal wavelength waves from the wavefield. This result is supported by the analysis of *Wu* [2001] which indicates that amplitude growth is scale dependent in the upper stratosphere showing less efficient propagation for large-scale waves.

[33] It should be noted that our observations are dominated by data at middle to high latitudes and thus the patterns observed may change with a more comprehensive geographical sampling. For instance, previous work by *Alexander et al.* [2002] and *Preusse et al.* [2006] has demonstrated that the equatorial maximum observed in short vertical wavelength gravity wave climatologies is related to low-frequency, long horizontal wavelength waves. Thus, some of the geographical patterns observed in Figures 9 and 10 toward the equator are likely to be related to this fact. However, the number of observations at very short horizontal separations limits our ability to examine whether changes in horizontal wavelength as a function of latitude explain some of the patterns in Figures 6 and 7. Examination of the relative removal of long versus short horizontal wavelength waves as a function of latitude could be very interesting and will be a focus of further study using an extended data set.

[34] One issue that this analysis has not been considered is the sensitivity of satellite observations to observational filtering which was originally discussed by *Alexander* [1998] and supported by observational data provided by *Preusse et al.* [2000]. Observational filtering associated with radio occultation technique and the impact of line of sight effects have previously been a particular focus of studies by *Lange and Jacobi* [2003], *McDonald and Hertzog* [2008], and *P. Alexander et al.* [2008] and indicate that RO observations can only observe a portion of the gravity wave spectrum. While a detailed analysis of this factor is beyond the scope of this study, it should be noted that observational filtering and the Doppler shifting of portions of wave spectrum into and out of the observational filter of the RO technique is likely to impact the measurements made and will contribute to the patterns observed. However, it should be noted that the analysis technique used in this study relies less on the removal of large vertical wavelength perturbations than many previous studies [*Tsuda et al.*, 2000] and therefore observational filtering may be less important in this analysis.

[35] In addition to providing information on gravity wave characteristics, the results described in section 3.1 and 3.2 provide information which can be used to define coincidence criteria for validation exercises. In particular, the analysis presented highlights that measurements separated in time by periods less than 5 hours must be used in validation exercises, though this is not a strong constraint for such validation studies which typically use observations separated in time by no more than 3 hours. In addition, an important point derived from Figure 5 was that for horizontal separations below 500 km the vast majority of the variability (between 60% and 90% of the variations in temperature observed) are likely to be associated with internal gravity waves. Since most validation exercises use paired observations separated by distances smaller than this range it seems that studies which aim to validate temperature observations must consider the main form of geophysical variability in their statistical analyses to be associated with gravity waves. Thus, the ability to make measurement of instrumental differences rather than geophysical variability will depend on geographic location since wave activity has seasonal and geographic variations. For example, validation exercises in the summer hemisphere stratosphere (see Figures 9 and 10) are likely to be less affected by geophysical variability than those in the winter hemisphere.

5. Conclusions

[36] Examination of the T_{RMS} between pairs of COSMIC observations separated by small horizontal distances (less than 1000 km) and short time differences (less than a few hours) shows clear seasonal patterns and variations as a function of altitude. Some of these variations in T_{RMS} can be related to changes in the background temperature field, while others are related to the gravity wavefield. For example, the strong changes in Figures 6 and 7 in the summer hemisphere seem to be related to variations in the makeup of the wavefield associated with critical level filtering. The much smaller changes observed in the winter patterns as a function of altitude are also suggestive of this possibility. The geographic variation observed in Figures 9 and 10 also demonstrates that the T_{RMS} metric is sensitive to the gravity wavefield since features previously highlighted in a number of climatologies are observed [*Tsuda et al.*, 2000; *Preusse et al.*, 2001; *Jiang et al.*, 2004; *Baumgaertner and McDonald*, 2007; *S. P. Alexander et al.*, 2008, 2009].

[37] The derivation of the second-order structure function (shown in Figures 6 and 7) from paired COSMIC profiles and their relationship to the horizontal wave number power spectra indicates that this paired observational methodology can derive gravity wave characteristics in a complementary way to other techniques. The generally good correspondence between the form of the second-order structure functions and horizontal wave number power spectra at higher [*Wu*, 2001] and lower altitudes [*Nastrom and Gage*, 1985] highlights the utility of this methodology. Analysis of the second-order structure functions also suggests that the wavefield may be particularly affected by changes in the zonal wind field between 15 and 25 km and that longer horizontal wavelength waves may be preferentially removed from the wavefield by critical level filtering in this region. Though the possibility of significant observational filtering also exists and will be the subject of a forthcoming paper. The analysis at low altitudes shows a remarkably similar pattern in both hemispheres which suggests that much of the seasonal variability observed at higher altitudes may be due to changes in the propagation conditions in the lower stratosphere. This concurs with many previous analyses, for

example, that of *Preusse et al.* [2008], which indicate that the wind reversal between tropospheric westerlies and stratospheric easterlies in the summer lower stratosphere strongly contributes to the critical-level filtering of small phase-speed waves.

[38] Examination of the variability as a function of spatial and temporal separation also demonstrates that gravity wave activity dominates the variability observed in stratospheric temperature at time and spatial scales often used in validation studies and that therefore gravity wave climatologies may provide useful information for the selection of validation data. For example, validation exercises in the summer hemisphere stratosphere are likely to be less affected by geophysical variability than those in the winter hemisphere.

[39] **Acknowledgments.** The authors would like to acknowledge the distribution of FORMOSAT-3/COSMIC data by CDAAC. A.J.M. would also like to acknowledge support provided by CIRES during his period as a visiting sabbatical fellow, during which period this work was completed. Support for the lidar observations was provided by the National Science Foundation, the British Antarctic Survey, and the University of Illinois at Urbana-Champagin. We thank C. S. Gardner, G. Papen, P. Espy, G. Nott, J. Diettrich, D. J. Maxfield, A. El Dakrouri, and J. Bird for their assistance in deploying the lidar. B.T. and X.C. were partially supported by NSF CAREER grant ATM-0645584.

References

Alexander, M. J. (1998), Interpretations of observed climatological patterns in stratospheric gravity wave variance, *J. Geophys. Res.*, *103*, 8627–8640.

Alexander, M. J., and C. Barnet (2007), Using satellite observations to constrain parameterizations of gravity wave effects for global models, *J. Atmos. Sci.*, *64*, 1652–1665.

Alexander, M. J., T. Tsuda, and R. A. Vincent (2002), Latitudinal variations observed in gravity waves with short vertical wavelengths, *J. Atmos. Sci.*, *59*, 1394–1404.

Alexander, M. J., et al. (2008), Global estimates of gravity wave momentum flux from High Resolution Dynamics Limb Sounder observations, *J. Geophys. Res.*, *113*, D15S18, doi:10.1029/2007JD008807.

Alexander, P., A. de la Torre, and P. Llamedo (2008), Interpretation of gravity wave signatures in GPS radio occultations, *J. Geophys. Res.*, *113*, D16117, doi:10.1029/2007JD009390.

Alexander, S. P., T. Tsuda, and Y. Kawatani (2008), COSMIC GPS observations of Northern Hemisphere winter stratospheric gravity waves and comparisons with an atmospheric general circulation model, *Geophys. Res. Lett.*, *35*, L10808, doi:10.1029/2008GL033174.

Alexander, S. P., A. R. Klekociuk, and T. Tsuda (2009), Gravity wave and orographic wave activity observed around the Antarctic and Arctic stratospheric vortices by the COSMIC GPS-RO satellite constellation, *J. Geophys. Res.*, *114*, D17103, doi:10.1029/2009JD011851.

Anthes, R. A., et al. (2008), The COSMOC/FORMOSAT-3—Mission early results, *Bull. Am. Meteorol. Soc.*, *89*, 313–333.

Bacmeister, J. T., S. D. Eckermann, P. A. Newman, L. Lait, K. R. Chan, M. Loewenstein, M. H. Proffitt, and B. L. Gary (1996), Stratospheric horizontal wavenumber spectra of winds, potential temperature, and atmospheric tracers observed by high-altitude aircraft, *J. Geophys. Res.*, *101*, 9441–9470.

Barlow, R. (1989), *Statistics: A Guide to the Use of Statistical Methods in the Physical Sciences*, John Wiley, Chichester, U. K.

Baumgaertner, A. J. G., and A. J. McDonald (2007), A gravity wave climatology for Antarctica compiled from Challenging Minisatellite Payload/Global Positioning System (CHAMP/GPS) radio occultations, *J. Geophys. Res.*, *112*, D05103, doi:10.1029/2006JD007504.

Cho, J. Y. N., R. E. Newell, and G. W. Sachse (2000), Anomalous scaling of mesoscale tropospheric humidity fluctuations, *Geophys. Res. Lett.*, *27*, 377–380.

Chu, X. Z., W. L. Pan, G. C. Papen, C. S. Gardner, and J. A. Gelbwachs (2002), Fe Boltzmann temperature lidar: Design, error analysis, and initial results at the North and South poles, *Appl. Opt.*, *41*, 4400–4410.

Davis, A., A. Marshak, W. Wiscombe, and R. Cahalan (1994), Multifractal characterizations of nonstationarity and intermittency in geophysical fields: Observed, retrieved, or simulated, *J. Geophys. Res.*, *99*, 8055–8072.

Eckermann, S. D., and P. Preusse (1999), Global measurements of stratospheric mountain waves from space, *Science*, *286*, 1534–1537.

Eidmann, G., D. Offermann, and P. Preusse (2001), Fluctuation power spectra in the mid stratosphere at increased horizontal resolution, in *Middle Atmosphere Temporal and Spatial Structures*, *Adv. Space Res.*, vol. 27, edited by M. Riese et al., pp. 1647–1652, Elsevier Sci., Amsterdam, Netherlands.

Eidmann, G., D. Offermann, B. Schaeler, M. Jarisch, and F. J. Schmidlin (2002), Stratospheric variability of temperature and ozone as inferred from the second CRISTA mission: Zonal means and local structures, *J. Geophys. Res.*, *107*(D23), 8180, doi:10.1029/2001JD000721.

Ern, M., P. Preusse, M. J. Alexander, and C. D. Warner (2004), Absolute values of gravity wave momentum flux derived from satellite data, *J. Geophys. Res.*, *109*, D20103, doi:10.1029/2004JD004752.

Hauchecorne, A., and M. L. Chanin (1980), Density and temperature profiles obtained by lidar between 35 and 70 km, *Geophys. Res. Lett.*, *7*, 565–568.

Hertzog, A., G. Boccara, R. A. Vincent, F. Vial, and P. Cocquerez (2008), Estimation of gravity wave momentum flux and phase speeds from quasi-Lagrangian stratospheric balloon flights. Part II: Results from the Vorcore campaign in Antarctica, *J. Atmos. Sci.*, *65*, 3056–3070.

Horinouchi, T., and T. Tsuda (2009), Spatial structures and statistics of atmospheric gravity waves derived using a heuristic vertical cross-section extraction from COSMIC GPS radio occultation data, *J. Geophys. Res.*, *114*, D16110, doi:10.1029/2008JD011068.

Jensen, A. S., M. S. Lohmann, H. H. Benzon, and A. S. Nielsen (2003), Full spectrum inversion of radio occultation signals, *Radio Sci.*, *38*(3), 1040, doi:10.1029/2002RS002763.

Jiang, J. H., B. Wang, K. Goya, K. Hocke, S. D. Eckermann, J. Ma, D. L. Wu, and W. G. Read (2004), Geographical distribution and interseasonal variability of tropical deep convection: UARS MLS observations and analyses, *J. Geophys. Res.*, *109*, D03111, doi:10.1029/2003JD003756.

Kahn, B. H., and J. Teixeira (2009), A global climatology of temperature and water vapor variance scaling from the Atmospheric Infrared Sounder, *J. Clim.*, *22*, 5558–5576.

Kitchen, M. (1989), Representativeness errors for radiosonde observations, *Q. J. R. Meteorol. Soc.*, *115*, 673–700.

Lange, M., and C. Jacobi (2003), Analysis of gravity waves from radio occultation measurements, in *First CHAMP Mission Results for Gravity, Magnetic and Atmospheric Studies*, edited by C. Reigber et al., pp. 479–484, Springer, Berlin.

Liou, Y. A., A. G. Pavelyev, S. F. Liu, A. A. Pavelyev, N. Yen, C. Y. Fluang, and C. J. Fong (2007), FORMOS AT-3/COSMIC GPS radio occultation mission: Preliminary results, *IEEE Trans. Geosci. Remote Sens.*, *45*, 3813–3826.

Lovejoy, S., A. F. Tuck, D. Schertzer, and S. J. Hovde (2009), Reinterpreting aircraft measurements in anisotropic scaling turbulence, *Atmos. Chem. Phys.*, *9*, 5007–5025.

Lu, C. G., and S. E. Koch (2008), Interaction of upper-tropospheric turbulence and gravity waves as obtained from spectral and structure function analyses, *J. Atmos. Sci.*, *65*, 2676–2690.

McDonald, A. J., and A. Hertzog (2008), Comparison of stratospheric measurements made by CHAMP radio occultation and Strateole/Vorcore in situ data, *Geophys. Res. Lett.*, *35*, L11805, doi:10.1029/2008GL033338.

Nastrom, G. D., and K. S. Gage (1985), A climatology of atmospheric wavenumber spectra of wind and temperature observed by commercial aircraft, *J. Atmos. Sci.*, *42*, 950–960.

Preusse, P., and M. Ern (2005), Indication of convectively generated gravity waves observed by CLAES, in *Coupling Processes in the Mlt Region*, *Adv. Space Res.*, vol. 35, edited by B. Clemesha and M. Taylor, pp. 1987–1991, Elsevier Sci., Oxford, U. K.

Preusse, P., S. D. Eckermann, and D. Offermann (2000), Comparison of global distributions of zonal-mean gravity wave variance inferred from different satellite instruments, *Geophys. Res. Lett.*, *27*, 3877–3880.

Preusse, P., G. Eidmann, S. D. Eckermann, B. Schaeler, R. Spang, and D. Offermann (2001), Indications of convectively generated gravity waves in crista temperatures, in *Middle Atmosphere Temporal and Spatial Structures*, *Adv. Space Res.*, vol. 27, edited by M. Riese et al., pp. 1653–1658, Elsevier Sci., Amsterdam, Netherlands.

Preusse, P., et al. (2006), Tropopause to mesopause gravity waves in August: Measurement and modeling, *J. Atmos. Sol. Terr. Phys.*, *68*, 1730–1751.

Preusse, P., S. D. Eckermann, and M. Ern (2008), Transparency of the atmosphere to short horizontal wavelength gravity waves, *J. Geophys. Res.*, *113*, D24104, doi:10.1029/2007JD009682.

Schmidt, T., A. de la Torre, and J. Wickert (2008a), Global gravity wave activity in the tropopause region from CHAMP radio occultation data, *Geophys. Res. Lett.*, *35*, L16807, doi:10.1029/2008GL034986.

Schmidt, T., J. Wickert, G. Beyerle, and S. Heise (2008b), Global tropopause height trends estimated from GPS radio occultation data, *Geophys. Res. Lett.*, *35*, L11806, doi:10.1029/2008GL034012.

Schreiner, W., C. Rocken, S. Sokolovskiy, S. Syndergaard, and D. Hunt (2007), Estimates of the precision of GPS radio occultations from the COSMIC/FORMOSAT-3 mission, *Geophys. Res. Lett.*, *34*, L04808, doi:10.1029/2006GL027557.

Sofieva, V. F., F. Dalaudier, R. Kivi, and E. Kyro (2008), On the variability of temperature profiles in the stratosphere: Implications for validation, *Geophys. Res. Lett.*, *35*, L23808, doi:10.1029/2008GL035539.

Sparling, L. C., J. C. Wei, and L. M. Avallone (2006), Estimating the impact of small-scale variability in satellite measurement validation, *J. Geophys. Res.*, *111*, D20310, doi:10.1029/2005JD006943.

Steiner, A. K., G. Kirchengast, B. C. Lackner, B. Pirscher, M. Borsche, and U. Foelsche (2009), Atmospheric temperature change detection with GPS radio occultation 1995 to 2008, *Geophys. Res. Lett.*, *36*, L18702, doi:10.1029/2009GL039777.

Tsuda, T., M. Nishida, C. Rocken, and R. H. Ware (2000), A global morphology of gravity wave activity in the stratosphere revealed by the GPS occultation data (GPS/MET), *J. Geophys. Res.*, *105*, 7257–7273.

Vincent, R. A., A. Hertzog, G. Boccara, and F. Vial (2007), Quasi-Lagrangian superpressure balloon measurements of gravity-wave momentum fluxes in the polar stratosphere of both hemispheres, *Geophys. Res. Lett.*, *34*, L19804, doi:10.1029/2007GL031072.

Wang, L., and M. J. Alexander (2009), Gravity wave activity during stratospheric sudden warmings in the 2007–2008 Northern Hemisphere winter, *J. Geophys. Res.*, *114*, D18108, doi:10.1029/2009JD011867.

Wu, D. L. (2001), Horizontal wavenumber spectra of MLS radiance fluctuations, *J. Atmos. Sol. Terr. Phys.*, *63*, 1465–1477.

Wu, D. L., and J. H. Jiang (2002), MLS observations of atmospheric gravity waves over Antarctica, *J. Geophys. Res.*, *107*(D24), 4773, doi:10.1029/2002JD002390.

Xiao, C. Y., X. Hu, and J. H. Tian (2009), Global temperature stationary planetary waves extending from 20 to 120 km observed by TIMED/SABER, *J. Geophys. Res.*, *114*, D17101, doi:10.1029/2008JD011349.

Yamashita, C., X. Z. Chu, H. L. Liu, P. J. Espy, G. J. Nott, and W. T. Huang (2009), Stratospheric gravity wave characteristics and seasonal variations observed by lidar at the South Pole and Rothera, Antarctica, *J. Geophys. Res.*, *114*, D12101, doi:10.1029/2008JD011472.

X. Chu and B. Tan, Cooperative Institute for Research in Environmental Sciences, University of Colorado, 216 UCB, Boulder, CO 80309-0216, USA.

A. J. McDonald, Department of Physics and Astronomy, University of Canterbury, Private Bag 4800, Ilam, Christchurch 8020, New Zealand. (adrian.mcdonald@canterbury.ac.nz)